AFRL-AFOSR-VA-TR-2021-0085

Twenty-four hour, horizon-to-horizon imaging with the AEOS and STARFIRE telescopes

Maberry, Michael
UNIVERSITY OF HAWAII SYSTEMS HONOLULU
2530 DOLE STREET SAK D-200
HONOLULU, HI, 96822-2309
US

07/27/2021
Final Technical Report

Air Force Research Laboratory
Air Force Office of Scientific Research
Arlington, Virginia 22203
Air Force Materiel Command

REPORT DOCUMENTATION PAGE

Form Approved
OMB No. 0704-0188

1. REPORT DATE *(DD-MM-YYYY)*	**2. REPORT TYPE**	**3. DATES COVERED** *(From - To)*
27-07-2021	Final	15 Jul 2014 - 14 Apr 2021

4. TITLE AND SUBTITLE
Twenty-four hour, horizon-to-horizon imaging with the AEOS and STARFIRE telescopes

5a. CONTRACT NUMBER

5b. GRANT NUMBER
FA9550-14-1-0178

5c. PROGRAM ELEMENT NUMBER
61102F

6. AUTHOR(S)
Michael Maberry

5d. PROJECT NUMBER

5e. TASK NUMBER

5f. WORK UNIT NUMBER

7. PERFORMING ORGANIZATION NAME(S) AND ADDRESS(ES)
UNIVERSITY OF HAWAII SYSTEMS HONOLULU
2530 DOLE STREET SAK D-200
HONOLULU, HI 96822-2309
US

8. PERFORMING ORGANIZATION REPORT NUMBER

9. SPONSORING/MONITORING AGENCY NAME(S) AND ADDRESS(ES)
AF Office of Scientific Research
875 N. Randolph St. Room 3112
Arlington, VA 22203

10. SPONSOR/MONITOR'S ACRONYM(S)
AFRL/AFOSR RTB1

11. SPONSOR/MONITOR'S REPORT NUMBER(S)
AFRL-AFOSR-VA-TR-2021-0085

12. DISTRIBUTION/AVAILABILITY STATEMENT
A Distribution Unlimited: PB Public Release

13. SUPPLEMENTARY NOTES

14. ABSTRACT
We've developed several novel imaging techniques that improve our ability to image through atmospheric turbulence. The use of these techniques will notably increase both the space-bandwidth product for diffraction-limited resolution performance and the available image contrast when performing speckle imaging with the Air Force's 3m-class telescopes. The increase in the space-bandwidth product means the Air Force will be able to monitor a larger sky area and for a more significant fraction of time than is currently achieved. The increase in image contrast will improve the Air Force's ability to observe faint objects due to their small size, distance away, or proximity to a much brighter object. The techniques, which capitalize on improving the synergy between how we collect and process images, include tomographic mapping of the wavefront using a single Shack-Hartmann sensor, dynamic aperture diversity, and a new optimization algorithm (Alternating Approximations).

15. SUBJECT TERMS

16. SECURITY CLASSIFICATION OF:			**17. LIMITATION OF ABSTRACT**	**18. NUMBER OF PAGES**	**19a. NAME OF RESPONSIBLE PERSON**
a. REPORT	**b. ABSTRACT**	**c. THIS PAGE**			MICHAEL YAKES
U	U	U	UU	19	**19b. TELEPHONE NUMBER** *(Include area code)* 00000000

Standard Form 298 (Rev.8/98)
Prescribed by ANSI Std. Z39.18

Twenty-four hour, horizon-to-horizon imaging with the AEOS and Starfire telescopes

Final Report for AFOSR Award FA9550-14-1-0178

Prinicpal Investigator: Michael Maberry, Email: *maberry@hawaii.edu*

Project Summary/Abstract

We've developed several novel imaging techniques that improve our ability to image through atmospheric turbulence. The use of these techniques will notably increase both the space-bandwidth product for diffraction-limited resolution performance and the available image contrast when performing speckle imaging with the Air Force's 3m-class telescopes. The increase in the space-bandwidth product means the Air Force will be able to monitor a larger sky area and for a more significant fraction of time than is currently achieved. The increase in image contrast will improve the Air Force's ability to observe faint objects due to their small size, distance away, or proximity to a much brighter object.

The techniques, which capitalize on improving the synergy between how we collect and process images, include tomographic mapping of the wavefront using a single Shack-Hartmann sensor, dynamic aperture diversity, and a new optimization algorithm (Alternating Approximations).

Glossary of Terms

Blind deconvolution: a restoration algorithm where both the object and a spatially invariant blurring function (point spread function or PSF) are determined from a blurred, noisy image of the object.

Multi-frame blind deconvolution (MFBD): blind deconvolution of a set of images where the object is stationary throughout the data set.

Myopic deconvolution: blind deconvolution augmented with wavefront sensor (WFS) data.

Speckle imaging: imaging an astronomical object with exposure times short enough to freeze the blurring effects of atmosphere.

Accomplishments

Here we briefly describe our research accomplishments under Award FA9550-14-1-0178. We limit ourselves to a concise summary and refer the reader to the publications listed in the section headings and at the end of this report for detailed developments.

1. Imaging through strong turbulence [P7, P19]

The project's overarching objective was to achieve diffraction-limited resolution performance with the Air Force's 3m-class telescopes when observing through the strong atmospheric turbulence

conditions experienced at low elevation angles and visible wavelengths. In addition to increasing the sky area that we can successfully monitor, the ability to observe through strong turbulence would also allow us to extend both our temporal coverage of the sky and the range of wavelengths we can use for observations.

A measure of the surveillance efficiency of a speckle imaging system that accounts for both the sky coverage and the fraction of time that we can make observations with diffraction-limited resolution is given by the "clear sky" space-bandwidth product

$$\mathrm{SBP} = \left[1 - \left(\frac{r_o^{min}}{r_0^{vert}}\right)^{5/3}\right]\left[1 - \int_0^{r_0^{min}} \chi_k^2(r_0^{vert} : k)dr_0\right] \quad . \tag{1}$$

The first term in brackets represents the sky coverage for values of r_0 such that $r_0 \geq r_0^{min}$, where r_0^{min} is the minimum value of r_0 for which the imaging system can deliver diffraction-limited resolution. The second term in brackets represents the temporal probability distribution function for r_0. We model this distribution using a chi-square distribution with $k = 4$ degrees-of-freedom which matches the observed distribution during the daytime at Haleakala [1]. We set the mean of the χ_k^2 distribution to $r_0^{vert} = r_0^{median}(1 - 2/9k)^{-3}$, where r_0^{median} is the median value of r_0 at the zenith.

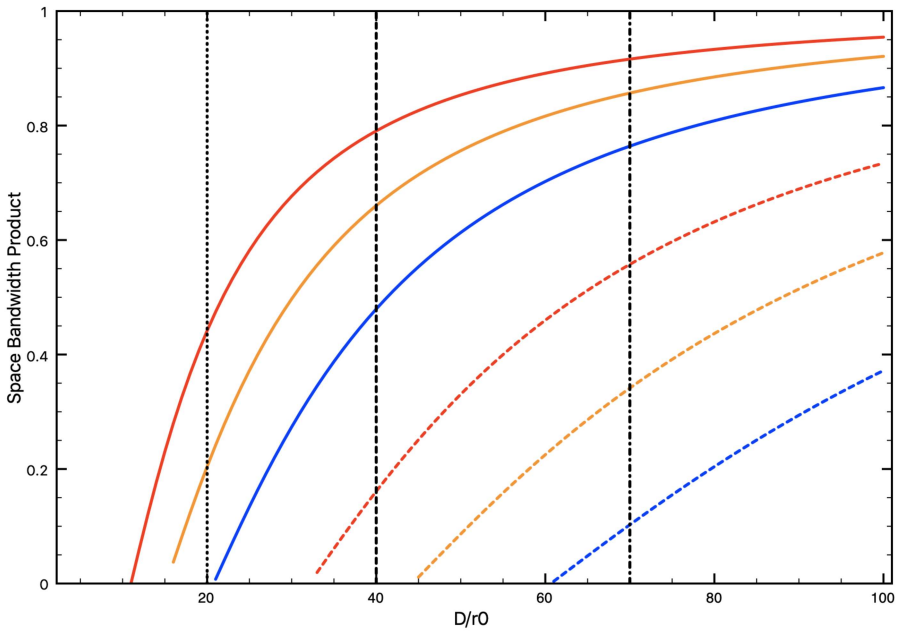

Figure 1: The clear sky space-bandwidth product for the AEOS 3.6m telescope at three wavelengths: 500 nm (blue), 650 nm (orange), and 850 nm (red), for median r_0 values of 5 cm (daytime - dashed lines) and 14.6 cm (nighttime- solid lines). The x-axis represents the maximum value of D/r_0 for which the imaging system can deliver diffraction-limited resolution imagery. The vertical lines indicate current capability (dotted), potential capability at beginning of award (dashed), and projected capability based on the results of this research (dot-dashed).

For observations at 500 nm at the Maui Space Surveillance Site (MSSS) in Hawaii, the median value of r_0 is around 5 cm during the daytime and 14.6 cm at nighttime (Fig. 10 in [2]). The

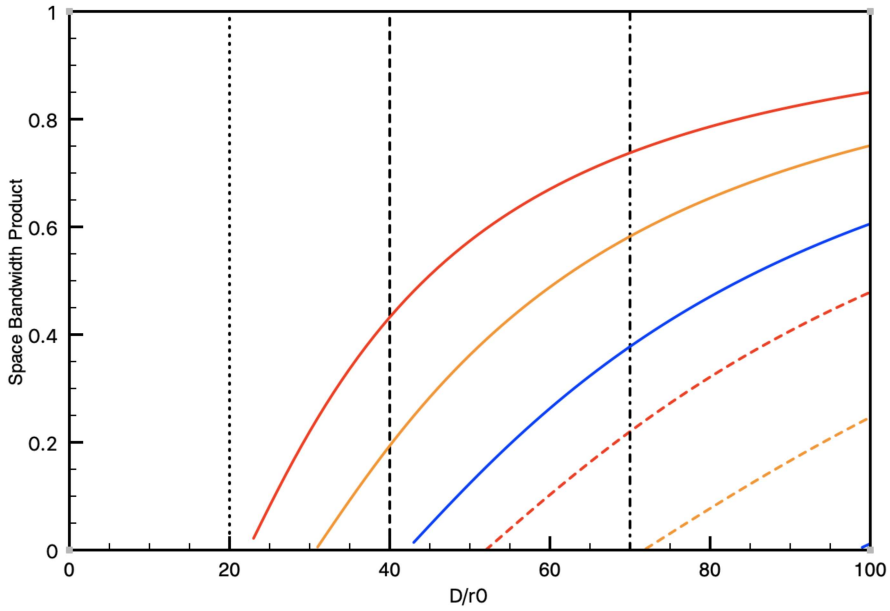

Figure 2: The clear sky space-bandwidth product for the Starfire 3.5m telescope. Here we use r_0 values of 3 cm for the daytime and 7 cm for the nighttime. These represent 'by eye' estimates of the median values. The other details for the figure are the same as in Fig. 1. We note that diffraction-limited performance at 500 nm for daytime conditions starts to be achievable at $D/r_0 = 99$.

seeing at the Starfire Optical Range (SOR) site in New Mexico site is generally not as good as the Hawaiian site. For SOR, we estimate median values of r_0 of around 3 cm for the daytime and 7 cm for the nighttime (Fig. 10 in [3]).
Figures 1 and 2 show the space-bandwidth product for speckle observations made with the AEOS 3.6m telescope at AMOS, and the Starfire 3.5m telescope at SOR, respectively, for a variety of wavelengths under the median day/night turbulence conditions for each site. These figures clearly show why observations are typically performed at near-IR wavelengths: the space-bandwidth product is substantially higher than it is at visible wavelengths. We note a space-bandwidth product of 1 indicates that diffraction-limited resolution images are continuously available for the entire sky during the day/night.

During this award we focused on building on our earlier work on aperture diversity [4] that allowed for imaging with diffraction-limited resolution through turbulence conditions of up to $D/r_0 = 40$. One advance we have made in this endeavor is we have shown using numerical simulations that optimal partitioning of the telescope aperture into annular sub-apertures depends on the turbulence conditions [P19]. Here we use the speckle transfer function associated with a given aperture as a measure of the information passed at each spatial frequency by the aperture. We then look for the set of sub-apertures that transmit the most information when viewed as a collective. The observed dependence of the optimal partitioning of the telescope aperture on the instantaneous turbulence conditions suggests that we should consider moving from static aperture diversity to dynamic aperture diversity when we want to achieve the best resolution and contrast for the post-processed image from a set of speckle data. In this scenario the configuration of the annular apertures would dynamically change as the atmospheric turbulence conditions change. For monochromatic imaging this could be achieved using spatial light modulators and polarization

optics.

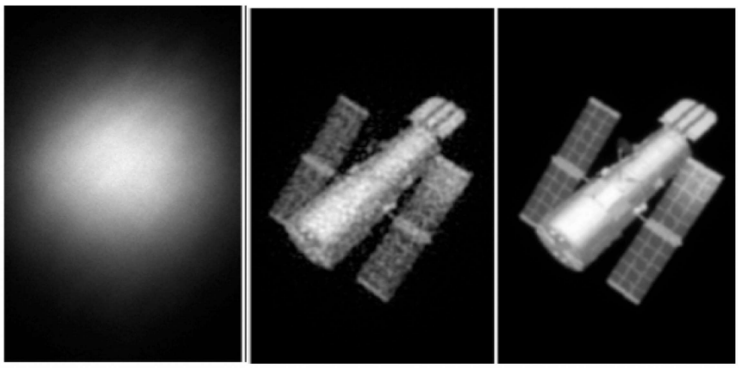

Figure 3: Left to right: a) example simulated data frame for $D/r_0 = 70$ with a target brightness of mv=+2 and a 2 ms exposure (x 0.5 zoom); b) CMFBD/MFBD restoration of 17 sets of 35 "aperture diverse" images that include three annuli and an imaging Shack-Hartmann WFS configuration of 32 sub-apertures; c) simulated diffraction-limited image for a 3.6 m telescope. The RMSE values for (b) and (c), with respect to the true image, are 0.23 and 0.19, respectively. Images are taken from publication P7.

By using the aperture partitioning schedule suggested by our numerical simulations for strong turbulence conditions, adopting the CMFBD/MFBD approach described under accomplishment #2 below, and the object refresh concept developed for our Alternating Approximations MFBD algorithm described in accomplishment #3 below, we can now achieve diffraction-limited resolution out to $D/r_0 = 70$ using our updated aperture-diversity algorithm (see Fig. 3).

Figures 1 and 2 show that the resulting improvement in the space-bandwidth product is significant: especially for the daytime observing conditions. Moreover, the improvement in imaging performance now makes observing at visible wavelengths a viable proposition, even during the daytime for the AMOS site.

Comments/Next Steps: The next step is to verify the results from our numerical simulations with bench top experiments. In addition, while our restoration algorithms perform well, the performance comes at a considerable time cost. The next step with the algorithms is to accelerate them to provide restorations at "the speed of relevance" for the Air Force's customers.

2. Restoration of large data sets [P4, P6, P15, P18]

When looking at faint targets, due to their size or distance away, we often require observing for periods of several tens of seconds or more. At the frame rates associated with speckle imaging, this results in data sets with thousands of images. In principle, the quality of an MFBD restoration should improve as the number of frames increases. However, as the number of frames increases, so does the number of variables required to model all the data. The estimation of the parameters then becomes impractical due to the large dimensionality of the parameter hyperspace. This shortcoming is manifest as entrapment in local minima during the optimization. The result is a sub-optimal restoration.

Compact MFBD (CMFBD) is an algorithm that we developed, under a previous award from AFOSR, to overcome this limitation when dealing with large data sets [5]. CMFBD models a subset of the data with high-SNR to estimate the object and the PSFs for the selected data frames, but

it uses all the data to constrain the PSF estimates. A limitation of this approach, which requires only a relatively small number of variables, is that the estimate of the object is based only on the information available in the subset of the data. The information on the object that is encoded in the frames outside of this subset is not used.

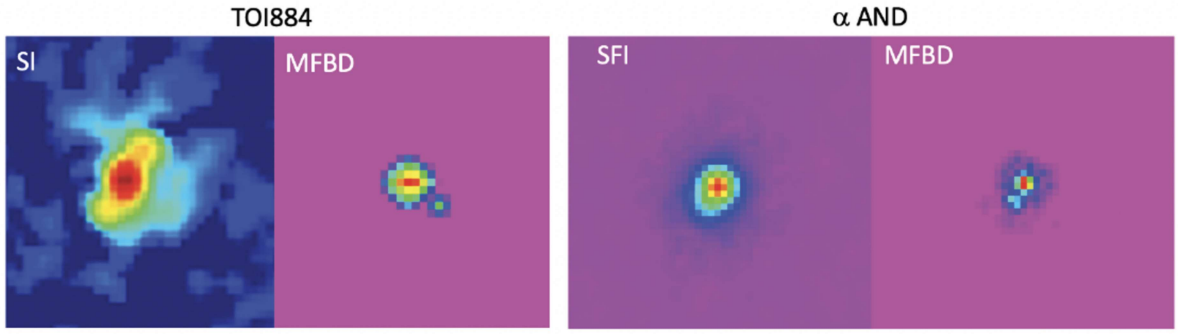

Figure 4: This figure demonstrates the performance of our baseline CMFBD/MFBD algorithm [P4] with speckle data acquired with 8m-class telescopes. The left-hand panel shows the results from an analysis of 1,000 frames of speckle data (60 ms exposures) of TOI884 obtained with the Alopeke instrument on the Gemini 8.1 m telescope. TOI884 is a mag +9.95 object with a companion at a separation of 48 mas and a contrast of Δm=+3. The images were acquired without AO compensation at 832 nm, and processed using standard speckle interferometry and our CMFBD/MFBD algorithm. The two images show the reconstructed objects (logarithmic scale) using each approach. The right-hand panel shows the reconstruction of 2,000 frames of AO-compensated data of Alpha Andromedae (α AND) acquired with the SHARK-VIS Forerunner instrument (1 ms exposures) on the 8.4m Large Binocular Telescope at 656 nm, and processed using the Speckle-Free Imaging (SFI) [6] algorithm (left) and our CMFBD/MFBD algorithm (right). α AND is a binary system with a mag +2 primary star and a companion at 16.9 mas with a contrast of Δm=+2. We note the diffraction-limited resolution for the observation is 19.7 mas. These images are shown with a square-root scaling. Right-hand panel is taken from publication P4.

In this award, we have improved on the original CMFBD concept in two ways. The first is that we have enhanced the CMFBD algorithm's performance by enforcing internal consistency in the estimated PSFs [P6]. The second is we use CMFBD as a precursor to MFBD [P4]. Here we generate an improved estimate of the object by performing a forward deconvolution of the complete data set using the estimated PSFs from CMFBD and the object estimate from CMFBD. The resultant object estimate and the CMFBD estimates for the PSFs then provide a good starting point for an MFBD restoration of the data. One which is less susceptible to entrapment in local minima during the restoration process.

We have demonstrated the advantage of this two-step CMFBD/MFBD approach using real data of unresolved and spatially resolved objects. Figs. 4 and 5 demonstrate the performance for high-resolution and high-contrast imaging of closely-spaced, unresolved objects (CSOs). We note that we estimated the complex wavefront for each image during the restoration process for the targets in Fig. 4. Although we obtained these results, which represent the state-of-the-art, for binary star systems using 8m-class telescopes [P4, P15], we can use them to infer the performance that we can expect for detecting CSOs with the Air Force's 3 m-class telescopes. We do this by increasing the observing times by the ratio of the areas of the apertures (see Table 1).

Star #1 [mag]	Star #2 [mag]	Separation [λ/D]	Observing time [sec]	Object
+2	+4	0.9	1.3	TOI884
+5.73	+13.98	5.3	12	Gliese 777 (*)
+9.95	+12.95	1.9	320	α AND

Table 1: Details of binary objects shown in Figs. 4 and 5, along with the observing times on a 3.5m telescope needed to achieve the same photon flux. The TOI884 and Gliese 777 objects represent reasonable proxies for LEO targets, while the object α AND represents a proxy for a GEO target. (*) - images were injected with artificial planetary signals.

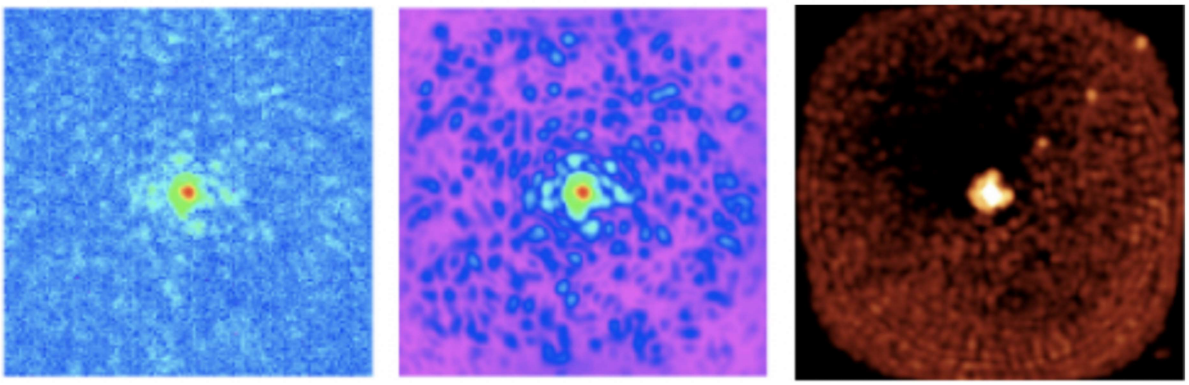

Figure 5: An example AO compensated speckle data frame of Gliese 777 (magnitude +5.73) acquired with the 8.4m Large Binocular Telescope (LBT) (left), and the corresponding model from the CMFBD/MFBD restoration of a 2,000 frame data set (middle). The right-hand image shows the recovered object. Here the dynamic range has been stretched to show the detection in the upper quadrant of artificial signals injected into the raw image data set at an intensity of 5.10^{-4} of the intensity of the central star (with a spacing of 100 mas). This stretching of the image contrast saturates the central star. Images are taken from publication P15.

Although it does not provide a demonstration of the processing of a large data set, Fig. 6 does show the improvement in the fidelity of the restored image of an extended object when using the CMFBD/MFBD approach. This figure shows the result of processing 271 speckle frames of the Seasat remote sensing satellite in LEO. The images were acquired without AO compensation with a 1.6m telescope at AMOS. When compared to the result from an MFBD restoration of the data, the gain in the sharpness of the solar panels and SAR antenna afforded by CMFBD/MFBD processing is apparent, as is the cleaner background.

We note that for objects whose power spectrum falls off with spatial frequency, which is the case for images of resolved artificial satellites, we can model the object using the same band-limited approach as is used for modeling the atmospheric PSF via the sampled wavefront in the telescope aperture. In addition to providing a physically motivated regularization on the object's spectrum during the restoration process, this approach has the additional advantage of requiring fewer variables to model the object than are needed for a pixel-by-pixel description in the object domain. This approach to modeling the object, which was proposed a number of years ago [7], has only been demonstrated using a binary object. The reason for this limitation was related to difficulties associated with providing initial estimates for the variables. We have overcome this

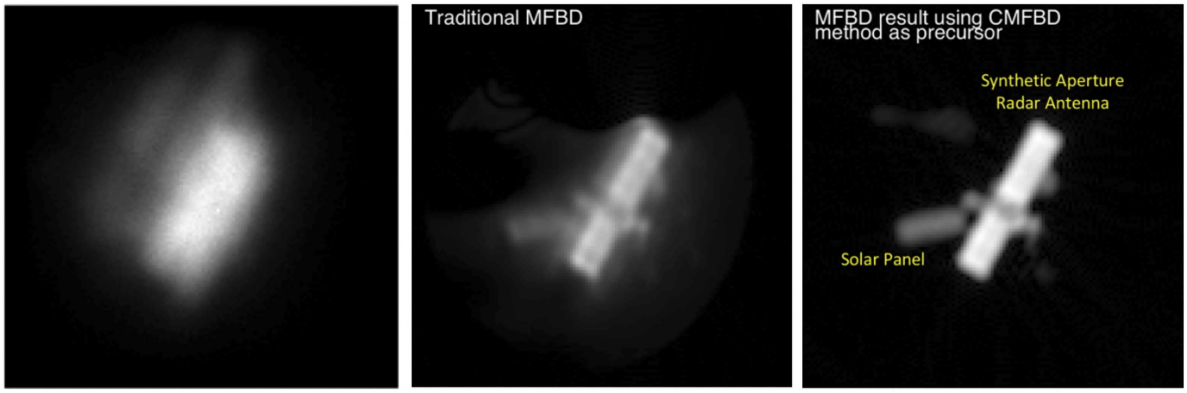

Figure 6: Raw speckle image of the Seasat remote sensing satellite observed with a 1.6m aperture telescope (left). Traditional MFBD restoration (middle) and CMFBD/MFBD restoration (right). Both restorations used 271 frames of data. All images are shown on a square root scale to emphasize the background. Images are taken from publication P6.

issue by generating an initial estimate of the object using a pixel-by-pixel model, solving for the commensurate (complex) "pseudo-pupil" variables, and then switching to these variables for the remainder of the restoration. At end of restoration when we are close to the solution, we switch back again. This allows for corrections to any errors in the power spectrum fall-off.

Comments/Next Steps: As demonstrated in Fig. 5, the CMFBD/MFBD algorithm performs well with a 2,000-frame data set. We are now investigating the practicalities of extending the technique to the tens of thousands of frames that are needed to achieve the highest contrast levels (10^6 and higher). Unfortunately, we have not been able to validate the performance of the CMFBD/MFBD algorithm for myopic deconvolution [8] of large (real) data sets due to lack of availability of scene-based SH WFS data. However, we expect to have such data in hand from the SHARK Forerunner instrument on the 8.4 m LBT, in the near future. The expectation is that the results highlighted in this section will be significantly improved by moving to myopic deconvolution.

3. Restoration of limited data sets [P10]

Not all objects remain stationary long enough to secure a large number of images for processing using an MFBD algorithm. Some objects change pose quickly and can only be considered stationary for very short periods. This lack of stationarity results in data sets with only a few frames (the limiting case being a single frame). Finding a high-quality solution to the blind restoration of a few images thus depends strongly on the performance of the optimization algorithm: a well-known weak link in the blind restoration process. .

To address this shortcoming we have developed a new approach to the optimization procedure: Alternating Approximations (AA).

The AA algorithm consists of addressing fixed points of an iteration in which both the object and the PSF are approximated in an alternating manner, *discarding* the previous approximation for the object when updating the PSF (and vice versa), and considering the resultant fixed points as candidates for a sensible solution. The alternating approximations are performed by truncated iterative least-squares descents in an inner minimization, where the number of descents in the object- and in the PSF-space plays a role of two regularization parameters. Selection of appropriate

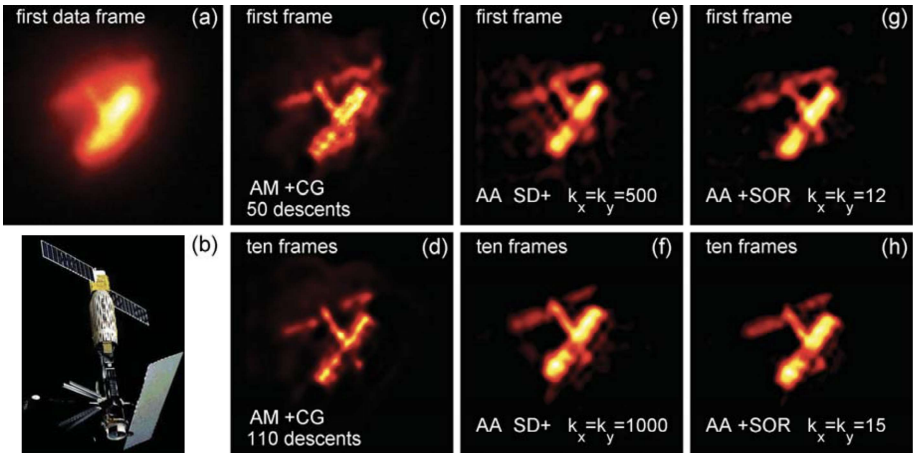

Figure 7: Deconvolution of speckle images of the remote sensing satellite Seasat. Top row: results for a single-frame restoration. Left-to-right: the first data frame (a), single-frame restorations with alternating minimization and conjugate gradients (CG) using 50 descents (c), alternating approximation using 500 descents with non-negativity constrained steepest descents (SD+) (e) and non-negativity constrained successive over-relaxation (+SOR) 12 descents (g). Here k_x and k_y are the number of object and PSF descents. Bottom row: results obtained for a 10-frame restoration using 110 descents in AM (d) , and 1000 (SD+) descents (f) and 15 (+SOR) descents (h) in AA. Panel (b) shows an artist's rendition of the true object (image credit: NASA). Images are taken from publication P10.

fixed points (which may not be unique) is performed by relaxing the regularization gradually, using the previous fixed point as an initial guess for finding the next one. This relaxation of the regularization brings an approximation of better spatial resolution.

We investigated two different routines for the inner minimization: non-negativity- constrained steepest descents (SD+), and non-negativity-constrained constrained successive over-relaxation (SOR+) with adaptive scheduling of the relaxation parameter. We then compared the results from our AA algorithm, with the different inner minimization algorithms, with an alternating minimization (AM) algorithm using conjugate gradients (CG). This latter approach is often used in blind deconvolution algorithms (e.g., the PCID algorithm [9]). For the tests we used real data acquired at AMOS using a 1.6m telescope to observe Seasat and the 3.6m AEOS telescope to observe HST. The results are shown in Figs. 7 and 8.

Both figures demonstrate that the AA technique provides a better restoration than the AM approach. The results obtained using alternating approximations have better resolution, wider dynamic range, and reveal no artifacts. In addition, the results of AA with SOR+ are the cleanest and have the widest dynamic range. Figure 7 shows that by using an alternating approximation approach we are able to produce high-quality blind restoration of a single image which is important for studies of targets that change pose rapidly. Interestingly, the use of SOR+ with the five-frame HST data set encountered an issue with the relaxation parameter: It saturated at small values thus indicating an inability of the inversion to reproduce low-frequency components in all the data frames simultaneously. A closer look at the problem revealed that the behavior of the relaxation parameter is caused by sporadic reflections of the sunlight from the protective shield of the satellite (glints), seen clearly as bright point-like spots in Fig. 8 with brightness changing between the neighboring data frames. That is, even though we are using only five data frames, the object does not remain stationary over the frames. For this reason, we performed the AA

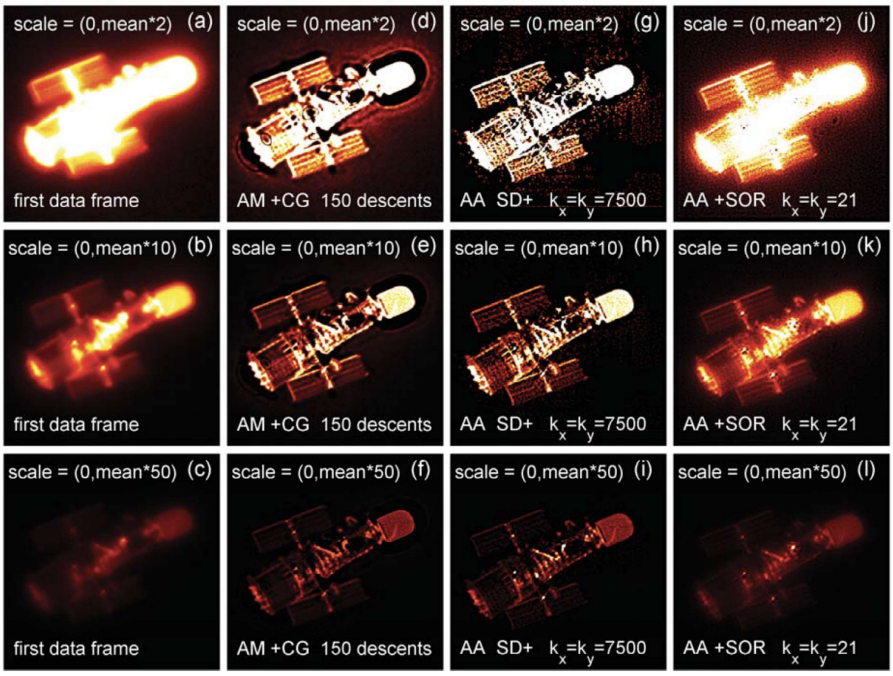

Figure 8: Deconvolution of a data set of five HST images, shown on three color scales with different thresholds: the scale which saturates at a level which is twice bigger than the mean pixel value in the corresponding image (panels in the upper row), 10 times bigger than the mean value (middle raw), and 50 times bigger (bottom rao). Panels of the first column show the first data frame, second column—the result of multi-frame deconvolution with AM, third column—multi-frame deconvolution with AA implementing SD+, and fourth column–the average of single-frame deconvolutions with AA using +SOR. The AA results were obtained using kx = ky = 7500 descents with SD+ and kx = ky = 21 descents with +SOR, the AM result implemented 150 descents. Images are taken from publication P10.

+SOR inversion for each individual frame, with further averaging of the results. However, what this exercise demonstrated is that our algorithm can detect when an object is non-stationary. This is an important capability when analyzing multiple frames simultaneously.

Comments/Next Steps: Incorporation of a band-limit constraint on the PSF estimation should improve performance. This is not a trivial exercise using the +SOR framework.

4. High-fidelity wavefront estimation for image post processing [P5]

We have shown that high-fidelity wavefront estimation is afforded by using an imaging Shack-Hartmann (ISH) wavefront sensor (WFS), along with a multi-aperture phase retrieval (MAPR) analysis of a time series of WFS data. The latter allows us to leverage the temporal correlations in the data which facilitates measurement of the high-spatial frequencies of the wavefront. Access to the high-spatial frequencies becomes increasingly important as the level of atmospheric turbulence increases. We capture the temporal correlations in the WFS data by modeling the atmosphere as a set of turbulence layers that are frozen and which propagate across the front of the telescope aperture at the local wind velocity at the height of each layer [10].

The performance of the ISH WFS/MAPR combination is demonstrated in Fig. 9 for a target

brightness of mag +7, which is approximately the brightness expected for a sodium laser guide star. This figure shows that we can recover the wave front phase with a residual root-mean-square error (rmse) of better than 0.35 radians over a wide range of turbulence conditions as measured using the ratio of the telescope aperture diameter (D) to the atmospheric coherence length (r_0). For reference, a rmse error of 0.47 radians or less corresponds to a Strehl of 0.8 and greater. These Strehl values are commonly accepted as representing diffraction-limited resolution. The error in the wavefront estimated from a MAPR analysis of ISH WFS data, is a significant improvement on that from a traditional Shack-Hartmann WFS that generates "spots" on the WFS camera, and determines the wavefront from the measured displacements of the spots from their position for a flat wavefront. The improvement is close to an order of magnitude at D/r_0=30. This improvement enables both high-contrast, high-resolution imaging of closely spaced objects, and the restoration of data through strong turbulence. The impact of the latter advance is that it greatly extends the space-bandwidth product for a site (see earlier), which translates to improved surveillance of the skies.

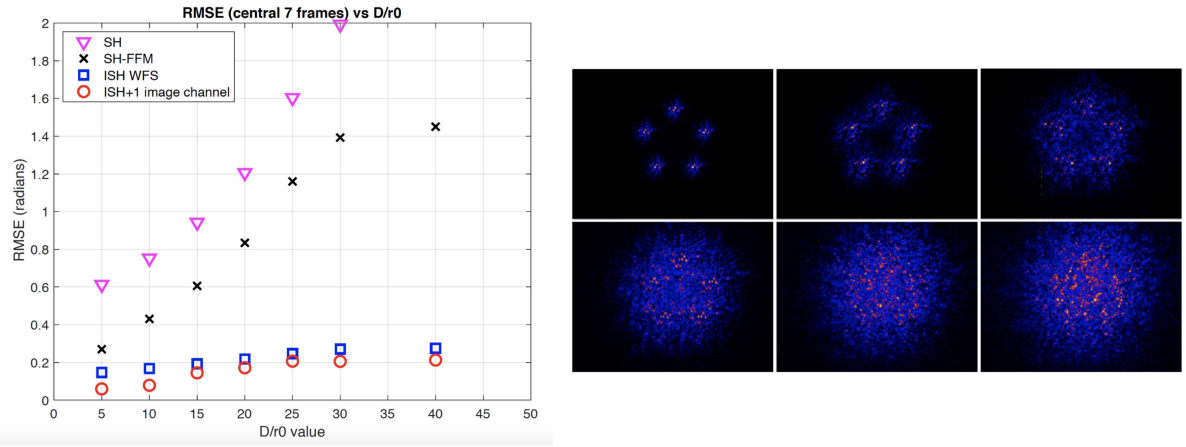

Figure 9: Left Panel: The tip/tilt removed wavefront errors based on simulations of a Shack-Hartmann wavefront sensor viewing a constellation of guide stars from a 50W sodium laser. The purple triangles show the performance of a traditional Shack-Hartmann WFS that samples the pupil with 32x32 sup-apertures and produces "spot" data. These data are typically used for real-time AO compensation. The black crosses show the same data processed as a time series to leverage the temporal correlations in the data. The blue squares show the results from using a time series of images from a scene-based (or "imaging") Shack Hartman WFS. The red circles show the improvement that comes from augmenting the WFS data, with data acquired with a second full-pupil imaging channel, in the restoration process with the full resolution of the aperture. Right Panel: The LGS constellation as observed in an imaging channel at turbulence levels of D/r_0 = 5, 10, 15, 20, 25, and 30 (starting in the top row and moving from left to right.

5. Tomographic mapping of the atmospheric wavefront [P3, P5, P14, P26]

Present techniques for the estimation of wavefront errors in three dimensions rely on multiple beacons, either natural stars or laser guide stars, to probe the atmospheric aberration along different lines of sight, followed by tomographic projection of the measurements. We have shown that tomographic mapping of the wavefront distortions imposed by the Earth's turbulent atmosphere can be obtained using a single beacon in *two* scenarios.

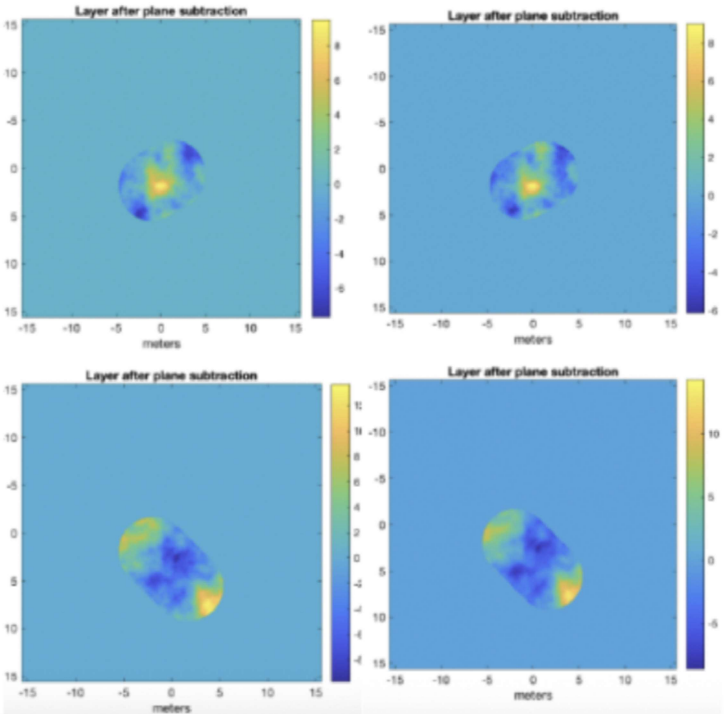

Figure 10: The global phases in each layer after subtraction of the best-fit "phase ramp." The truth phases, generated using an anisoplanatic model, are shown in the left column, and the recovered phases, based on recovery with an isoplanatic model, in the right column. The top row represents the ground layer (h=0) and the bottom row represents the high altitude layer (h=10 km). The length of each phase screen depends on the wind velocity for the layer ($V_{0km} = 5\ ms^{-1}, V_{10km} = 28\ ms^{-1}$).

The first scenario is when the atmosphere exhibits frozen flow behavior in different layers. This mechanism was first suggested by our research under a previous award from AFOSR which indicated that the frozen flow behavior of the atmosphere may allow for separation of the wavefront perturbations incurred at different heights in the atmosphere [4]. We have now verified that this is indeed the case when Shack-Hartmann WFS data are processed as a time series instead of on an image-by-image basis, which is the typical approach to wavefront estimation [P5]. Both for "spot" and "scene-based" Shack-Hartmann WFS data (Fig. 10).

Accurate estimation of the wavefront in the different layers not only facilitates improved estimation of the wavefront in the entrance pupil to the telescope, as we saw in the previous section, it also opens the door for tomographic mapping of the atmosphere. All that is needed for tomography is knowledge of the layers' heights. Fortunately, as the ISH WFS data are images, they contain this information which can be extracted through accurate modeling of the sub-aperture images. The layers' height determination requires three steps. In the first step we find the heights at which the layers provide models of the image data that best match the observed images. In the second step, the phase ramps across each global phase screen, which may have some small systematic error due to errors in the determination of the true location of the beacon in the field-of-view, are updated to improve the comparison between the model and observed images. In the third step, we update our estimate for the morphology of the beacon holding the wavefront phases constant and located at their estimated heights. These three steps are iterated until convergence, at which point we have all the information we need for 3-D tomographic mapping of the atmospheric wavefront. We also have a good low-spatial frequency estimate of the beacon.

Interestingly, we've found that the accuracy of the ISH WFS/MAPR combination improves as the spatial extent of the beacon increases. This property allows for the use of a wide range of beacons: from the target under observation, to an "elongated spot" whose elongation varies across the pupil, as is experienced when using sodium laser guide stars [11].

The second mechanism for tomographic wavefront sensing using a single beacon is more specific and is provided when the telescope tracks an object across the sky with non-uniform angular velocity [P3]. This is generally the case for observations of artificial earth-orbiting satellites. In principle, this approach could benefit from the leverage provided by the frozen flow behavior of the atmosphere.

Comments/Next Steps: The ability to accurately determine the wavefront at different heights in the atmosphere means that we can compute accurate PSFs for any location in the image: an important consideration when the field-of-view large enough that the PSF varies with spatial location.

A common approach for dealing with spatially varying blur is to segment the image and perform blind deconvolution on the separate image pieces. After the deconvolution step, we either sew the restored image segments together [12] or interpolate between the PSF estimates for each image piece and perform a global restoration [13]. In our experience, the latter procedure provides a better quality recovery. As the PSF estimates obtained using the tomography approach described above offer much higher quality than those determined by segmenting the image, we can expect solid advances in the restorations of image data acquired with a wide field of view. The next steps are to verify this conjecture and develop a myopic deblurring algorithm that can update the PSFs during the restoration process.

6. Detection of faint targets during the daytime [P2, P13, P20]

The challenge of detecting and characterizing targets that are faint, is exacerbated for observations taken during daylight hours. Similar to nighttime observations, once a target is too faint to be used as a beacon for wavefront sensing, we need to resort to providing a beacon. For daytime imaging the preferred beacon is a sodium laser guide star, due to the high altitude of the beacon. The bright sky background during the daytime, however, strongly degrades the signal-to-noise ratio (SNR) for wavefront sensing using typical narrowband filters.

One way to improve the SNR is to use a sodium magneto-optical filter (MOF) as a part of the WFS. An MOF comprises an atomic filter placed between crossed polarizers. With high-quality polarizers we can then reduce the background light, that is, light not at the frequency of the sodium D_2 transition, to a fraction of the intensity of the sodium laser guide star (see Fig. 12). Moreover, the MOF signal is relatively insensitive to changes in the daytime sky intensity.

Using a 6.5 W sodium laser to produce a guide star in the Earth's mesosphere, we find the return photon flux, as measured through a sodium magneto-optical filter, during daylight conditions is 1.2x10^6 photons/m^2/s^{-1} (Fig. 12). This suggests we can get $\sim 10^4$ photons m^{-2} ms^{-1} from a 50 W laser.

Comments/Next Steps: Upgrade the multi-aperture phase retrieval algorithm that we use for processing ISH WFS data to estimate the wavefront perturbations seen by a distant target but which are not fully sampled by sodium laser guide star. An advantage of our WFS algorithm is that it can accommodate changes in the morphology of the beacon that occur at different locations in the pupil.

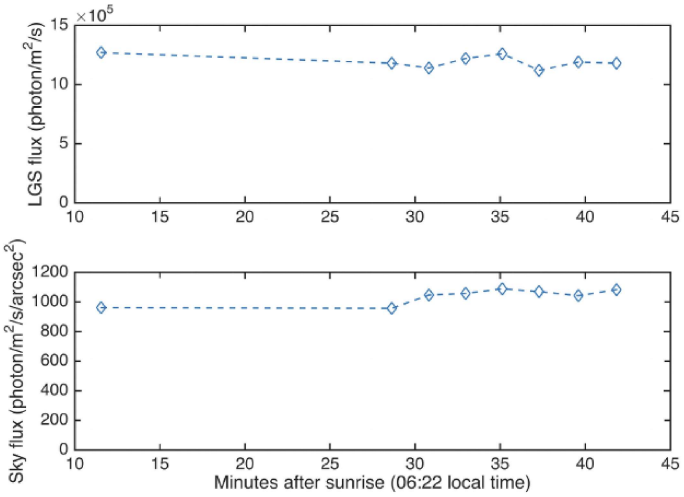

Figure 11: These plots are taken from publication P2.

7. Novel approaches to satellite characterization

The research effort conducted under this award revealed three promising research areas outside of the original proposed research topics but still within the general scope of the main research topic.

Hyper-spectral speckle imaging [P1, P11]

We have unveiled the possibility of using diffraction from the telescope's aperture and dispersion in the Earth's atmosphere to provide low-spectral resolution hyper-spectral images from ultra-broadband speckle data (600 nm spectral bandpass). Preliminary studies using a simple object (two closely spaced unresolved objects) indicate that it may be feasible to decode the spectral information contained in each pixel of the restored image of the object (see Fig. 13). Potential benefits include improved detection and characterization of the smallest objects on orbit, and the prospect of studying how materials age in space

Detecting satellite vibrations

Dopplergraphs based on magneto-optical filters (MOFs) have been demonstrated to be sensitive imaging instruments for measuring small oscillatory signals from targets outside the Earth's atmosphere. To investigate the potential for using such an instrument with the Air Force's 3m-class telescopes to detect the variations in the light reflected from satellites which are caused by their internal and external vibrations, we we used a funding plus-up to the award to build a demonstrator dual channel Dopplergraph running magneto-optical filters (MOFs) in the sodium and potassium D lines. The instrument was designed for use with the AEOS telescope on Maui (see Fig. 14). If such variations can be detected they could be used to seismically determine the dynamics and structure of the targets that can't otherwise be determined via passive remote sensing. For example, the level of fuel onboard a spacecraft and its size/mass.

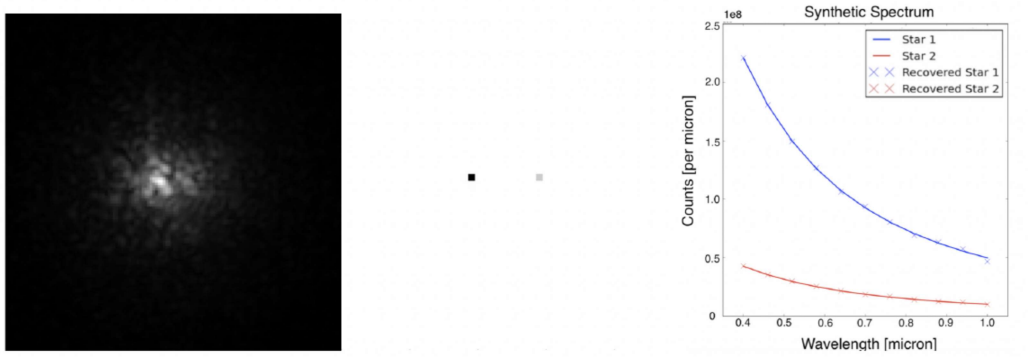

Figure 12: Left: A simulated speckle image of a binary star obtained over the spectral range 0.4 μm to 1 μm through median atmospheric turbulence conditions for the AMOS site on Haleakala, Hawaii, using the AEOS 3.5m telescope. Dispersion in the atmosphere has not been included. Center: Object at 0.4 μm reconstructed from 11 images taken at different times (without photon and read noise) and assuming perfect knowledge of the atmospheric wavefront at 0.5 μm for each image. The image has the same spatial scale as the image on left, and is shown with an inverted color table to enhance the visibility of both stars. As can be seen, the two stars are fully resolved with high contrast: the recovery is essentially perfect. The same is true for the other 10 wavelength bands. Right: The reconstructed spectra for each component of the binary star compared with the true spectra (blackbody curves). For this simple crude proof-of-concept, the integrated spectral signature was built using 11 wavelengths (each representing a "color plane" of the object), and the restoration solved for 11 color planes. These images and plot are taken from publication P11.

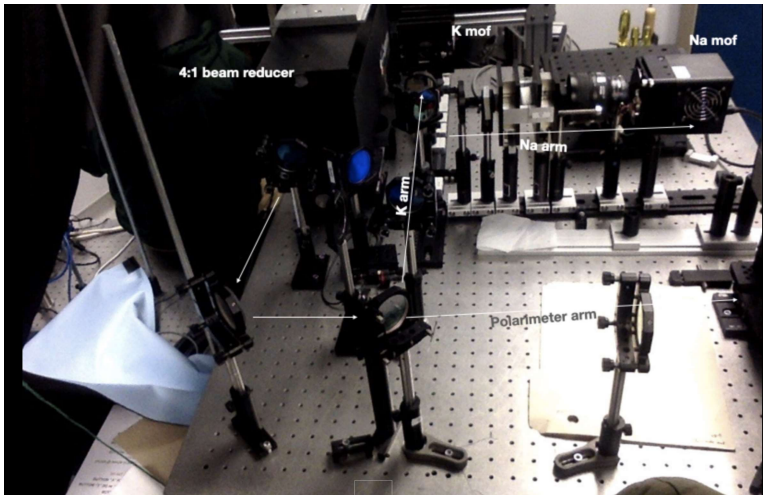

Figure 13: The dual-channel, magneto-optical filter-based Doppler magnetograph on the AEOS telescope.

Restoration-free imaging using machine learning [P25]

Restoration of satellite imagery that has been severely distorted by the Earth's turbulent atmosphere is a computationally demanding procedure that is typically not amenable to real-time analysis when the highest levels of resolution and contrast are needed. Restoration, however, is only an intermediate step towards more succinct goals, such as identifying the satellite model, orientation,

health, and intent. To the human eye, image restoration is an unavoidable prior to extracting these satellite characteristics, as our brains are not trained to distinguish between distorted images directly. However, the fact that restoration is even possible suggests that all the necessary information to recover the desired characteristics is indeed embedded in the distorted images, only encoded in a different way due to the light diffraction patterns produced by the atmosphere. Hence, we hypothesize that by training a deep convolutional neural network (D-CNN) to interpret distorted images directly, we can recover the desired satellite characteristics (e.g., model and orientation) in one step, with no need for image restoration nor further processing.

Our initial results in this endeavor show promise and indicate that some objects in are much easier to discern than others, with five classes showing more than 90% accuracy at the highest level of distortion. This is an encouraging start but significantly more research needs to be performed before we can achieve comprehensive characterization and real-time satellite characterization.

Comments/Next Steps: The first two studies have been picked up for further evaluation through awards from AFOSR and AFRL, respectively. Government contractors that work closely with the Air Force on Maui have expressed interest in collaborating on extending the third study.

Personnel

The following is a list of individuals who have worked on research supported in whole or in part by the Air Force Office of Scientific Research under Grant FA9550-14-1-0178:

- Mr. Amar Dhada, Georgia State University (undergraduate)
- Mr. Ryan Hall, Georgia State University, (graduate student - Ph.D. in progress)
- Dr. Douglas A. Hope, Georgia State University and Georgia Tech Research Institute
- Prof. Stuart M. Jefferies, Georgia State University
- Mr. Allister Knox, Georgia State University (Research Engineer)
- Mr. Dmitriy Shcherbik, Georgia State University (Research Engineer)
- Mr. Cody Smith, Georgia State University (undergraduate)
- Mr. Anderson Thrasher, Georgia State University (undergraduate)
- Mr. Ashish Tiwari, Georgia State University (graduate student, Masters)
- Mr. Thomas Tidrick, Georgia State University (undergraduate)
- Mr. Ryan Walden, Georgia State University (undergraduate)
- Dr. Matthew Willson, Georgia State University (postdoc)

Collaborators

- Prof. Michael Hart, University of Arizona
- Prof. James Nagy, Emory University
- Dr. Sergei Vorontsov, Queen Mary College, University of London, England

- Dr. Gianluca Li Causi, INAF – Istituto Nazionale di Astrofisica, Italy
- Dr. Fernando Pedichini, INAF – Istituto Nazionale di Astrofisica, Italy
- Dr. Marco Landoni, INAF – Istituto Nazionale di Astrofisica, Italy

Publications

The publications listed below represent papers supported in whole or in part by the Air Force Office of Scientific Research under Grant FA9550-14-1-0178:

Refereed Journals:

P1. Hall, R. and Jefferies, S. M. 2021, "Hyper-spectral speckle imaging for space situational awareness" Journal of Astronautical Sciences, submitted.

P2. Hart, M., Jefferies, S. M. and Murphy, N. 2016, "Daylight operation of a sodium laser guide star for adaptive optics wave-front sensing", Journal of Astronomical Telescopes, Instruments and Systems, 2(4), 040501, DOI: https://doi.org/10.1117/1.JATIS.2.4.040501, 26 Oct 2016

P3. Hart, M., Jefferies, S. M. and Hope, D. A. 2016, "Atmospheric tomography for artificial satellite observations with a single guide star", Optics Letters, 41, 3723-3726, DOI: https://doi.org/10.1364/OL.41.003723, 15 Aug 2016

P4. Hope, D. A., Jefferies, S. M., Li Causi, G., Landoni, M., Stangolini, M., Pedichini, F. and Antoniucci, S., "Post-AO high-resolution imaging using the Kraken multi-frame blind deconvolution algorithm", Ap.J., submitted (June 2021)

P5. Hope, D. A., Jefferies, S. M., Thrasher, A. and Tidrick, T., "Deblurring speckle images using scene-based Shack-Hartmann sensor data", Ap.J., in preparation (submission August 2021)

P6. Hope, D. A., Jefferies, S. M., and Smith, C. 2019, "High-fidelity imaging using compact multi-frame blind deconvolution", Journal Astronautical Sciences, 66, 162-169, DOI: https://doi.org/10.1007/s40295-018-00148-x, 15 March 2019

P7. Hope, D., Jefferies, S. M., Hart, M. and Nagy, J. 2016 "High-resolution speckle imaging through strong atmospheric turbulence", Optics Express, 24, 12116-12129, DOI: https://doi.org/10.1364/OE.24.012116, 30 May 2016

P8. Stangalini, M., Li Causi, G., Pedichini, F., Antoniucci, S., Mattioli, M., Christou, J., Consolini, G., Hope, D., Jefferies, S. M., Piazzesi, R., and Testa, V., 2018, "Recurrence quantification analysis as a post-processing technique in adaptive optics high-contrast imaging", Ap.J., 868, 6, DOI: https://doi.org/10.3847/1538-4357/aae58e, 13 Nov 2018

P9. Swindle, R., Hope, D., Hart, M., and Jefferies, S. 2018, "High Resolution SSA Imaging using Carbon Fiber Telescopes", Journal of Applied Remote Sensing, 12, 4, 042406, DOI: https://doi.org/10.1117/1.JRS.12.042406, 25 Sept 2018

P10. Vorontsov, S. V. and Jefferies, S. M. 2017, "A new approach to blind deconvolution of astronomical images", Inverse Problems, 33, 5, 055004, DOI: https://doi.org/10.1088/1361-6420/aa5e16, 3 March 2017 (*)

* - This paper was selected for the journal's 2017 Highlights collection: http://iopscience.iop.org/journal/0266-5611/page/Highlights%20of%202017

Conference Proceedings:

P11. Hall, R. and Jefferies, S. M. 2020, "Ultra broadband high-contrast, high-resolution speckle imaging," AMOS Conference, Wailea, Maui, Sept 15-18, id.31, web: https://amostech.com/2020-technical-papers/

P12. Hart, M., Jefferies, S.M., Hope, D. A., Nagy, J. 2016, "A comprehensive approach to high-resolution daylight imaging for SSA", Proceedings of the Advanced Maui Optical and Space Surveillance Technologies Conference, held in Wailea, Maui, September 2016, Ed: S. Ryan, The Maui Economic Development Board, id.3

P13. Hart, M., Jefferies, S. M., and Murphy, N. 2016, "Daylight operation of a sodium laser guide star", Proc. SPIE 9909, Adaptive Optics Systems V, 99095N, DOI: https://doi.org/10.1117/12.2235080, July 2016

P14. Hart, M., Jefferies, S. M. and Hope D. 2016, "Tomographic wave-front sensing with a single guide star", Proc. SPIE 9982, Unconventional Imaging and Wavefront Sensing XII, 998207, DOI: https://doi.org/10.1117/12.2257358 , November 2016

P15. Hope, D. A., Jefferies, S. M., Stangalini, M., Pedichini, F., Li Causi, G., Mattioli, M., and Antoniucci, S. 2019, "High-resolution, high-contrast, imaging of small objects near satellites", AMOS Conference, Wailea, Maui, Sept 17-20, id.2

P16. Hope, D. A. and Jefferies, S. M., 2018, "Estimating the complex atmospheric wave front from speckle images", AMOS Conference, Wailea, Maui September 11-14, id.1

P17. Hope, D. A., Hart, M., Swindle, R., and Jefferies, S. M. 2017, "Image restoration from limited data", AMOS Conference, Wailea, Maui September 19-22 2017, id.86

P18. Jefferies, S. M., Hope, D. A. and Smith, C. 2017, "High-fidelity imaging using compact multi-frame blind deconvolution", AMOS Conference, Wailea, Maui September 19-22, 2017, id.5

P19. Jefferies, S. M., Knox, A., Dhada, A., Abbott, C., and Hope, D. A. 2017, "Dynamic aperture diversity", AMOS Conference, Wailea, Maui September 19-22, 2017, id.92

P20. Jefferies, S. M., Hart, M, Hope, D. A., and Murphy, N. 2016, "Daylight Operation of a Sodium Laser Guide Star for Adaptive Optics Wave-Front Sensing," Proceedings of the Advanced Maui Optical and Space Surveillance Technologies Conference, held in Wailea, Maui, September 2016, Ed: S. Ryan, The Maui Economic Development Board, id.2

P21. Pimentel-Alarcon, D., Tiwari, A., Jefferies, S. M., and Hope, D. A. 2018, "Leveraging machine learning for high-resolution restoration of satellite imagery", AMOS Conference, Wailea, Maui September 11-14, id.2

P22. Stangalini, M., Li Causi, G., Pedichini, F., Antoniucci, S., Mattioli, M., Christou, J., Consolini, G., Hope, D., Jefferies, S. M., Piazzesi, R., and Testa, V., 2018, "Recurrence quantification analysis as a post-processing technique in adaptive optics high-contrast imaging", Astronomical Telescopes and Instrumentation, SPIE, Austin, TX, June 2018, Proceedings of the SPIE, Volume 10703, id. 107032V, DOI: https:/doi.org/10.1117/12.2313355, July 2018

P23. Swindle, R., Hope, D., Hart, M., and Jefferies, S. 2018, "High-resolution Imaging of Satellites in Daylight", AMOS Conference, Wailea, Maui September 11-14, id.125

P24. Swindle, R., Hope, D. A., Hart, M., and Jefferies, S. M. 2017, "High-resolution SSA imaging using carbon telescopes", AMOS Conference, Wailea, Maui, September 19-22, 2017, id.1

P25. Walden, R., Dosunmu, T., Jefferies, S. M., and Pimentel-Alarcon, D. 2020, "Satellite characterization via restoration-free imaging: a novel machine learning paradigm for SSA", AMOS Conference, Wailea, Maui, Sept 15-18, id.28

P26. Willson, M., Jefferies, S. M., and Hope, D. A. 2018, "Tomographic Wave Front Sensing using a Single Imaging Shack-Hartmann Wave Front Sensor and Multi-Frame Blind Deconvolution", AMOS Conference, Wailea, Maui September 11-14, id.70

Research Products

We have developed two products that could be transitioned into operational use.

Kraken Image Restoration Software Package: The Kraken software package contains our basic CMFBD/MFBD algorithm, multi-aperture diversity algorithm (including use of Shack-Hartmann WFS data), and deblurring from wavefront sensing algorithm.

Dual-channel Dopplergraph: A dual-channel Doppler magnetograph system running magneto-optical filters (MOFs) in the sodium and potassium D lines is currently installed in the LANDIT telescope system at AMOS on Maui. This base system could also be used for other types of MOFs. For example, MOFs using Xenon and/or Nitrogen would have application for sensitive thruster plume detection.

Bibliography

1. T. Rimmele 1996, "Haleakala turbulence and wind profiles used for adaptive optics performance modeling", ATST Project Document RPT-0300.

2 L. W. Bradford 2010, Maui4: a 24 hour Haleakala turbulence profile, Advanced Maui Optical and Space Surveillance (AMOS) Technologies Conference September 2010, id5.

3 Earl J. Spillar, Marjorie A. Shoemake and Ann C. Slavin 2011, SAM, the Starfire Optical Range Atmospheric Monitor, Publications of the Astronomical Society of the Pacific Vol. 123, No. 908, 1210-1217

4 Final report for AFOSR Award FA9550-09-1-0216 /http://citeseerx.ist.psu.edu/viewdoc/download?doi=10.1.1.1032.3529&rep=rep1&type=pdf

5 D. A. Hope and S. M. Jefferies 2011, "Compact multi-frame blind deconvolution", Optics Letters, 36, 867-869

6 Gianluca Li Causi, Marco Stangalini, Simone Antoniucci, Fernando Pedichini, Massimil-iano Mattioli, and Vincenzo Testa 2017, SFADI: The Speckle-free Angular Differential Imaging Method. ApJ, 849.2, 85

7. Noriaki Miura 2003, Blind deconvolution under band limitation, Optics Letters ,Vol. 28, Issue 23, 2312-2314

8. Laurent M. Mugnier, Clelia Robert, Jean-Marc Conan, Vincent Michau, and Selim Salem 2001. "Myopic deconvolution from wave-front sensing". In: J. Opt. Soc. Am. A 18.4, 862–872.

9. Matson, C. L., Borelli, K., Jefferies, S. M., Hege, Beckner, C. C., E. K. and Lloyd-Hart, M. 2009, A Fast and Optimal Multi-Frame Blind Deconvolution Algorithm for High Resolution, Ground-Based Imaging of Space Objects, Applied Optics, 48, A75-A92

10. Jefferies, S. M. and Hart, M. 2011, "Deconvolution from wave front sensing using the frozen flow hypothesis", Optics Express, 19, 1975-1984

11. Beckers, J. M. 1992, Overcoming perspective elongation effects in laser-guide-star-aided adaptive optics, Appl. Optics, 31, 6592

12. Bardsley, Johnathan, Jefferies, Stuart, Nagy, James and Plemmons, Robert 2006, A computational method for the restoration of images with an unknown, spatially-varying blur, Optics Express, 14, 1767-82

13. Nagy, James G. and O'Leary, Dianne P. 1998, Restoring Images Degraded by Spatially Variant Blur, SIAM Journal on Scientific Computing, 19(4), 1063-1082